RSC Advances

PAPER

View Article Online
View Journal | View Issue

Check for updates

Cite this: *RSC Adv.*, 2025, **15**, 17302

Transforming invasive weeds into energy solutions: water hyacinth-based hybrid electrodes for green supercapacitors†

Shilpa Simon, Anila Rose Cherian and Sreeja P. B *

The excessive proliferation of *Eichhornia crassipes* (water hyacinth) poses significant environmental challenges; however, its abundant biomass offers a sustainable solution for energy storage applications. This study presents an eco-friendly approach to fabricating high-performance supercapacitor electrodes using water hyacinth-derived activated carbon (WH), polypyrrole (PPy), and titanium dioxide (TiO_2). The WH–TiO_2/PPy hybrid electrode was synthesized *via* hydrothermal treatment and interfacial polymerization, ensuring a resource-efficient and environmentally responsible process. The composite exhibited a high gravimetric capacitance of 610 F g^{-1} at 0.5 A g^{-1} in 3 M KOH, with excellent cycling stability (94% retention after 5000 cycles). An asymmetric supercapacitor with WH–TiO_2/PPy as the positive electrode and activated carbon as the negative electrode delivered an energy density of 98 W h kg^{-1} and a power density of 5606 W kg^{-1}. This work highlights the potential of transforming invasive biomass into cost-effective, high-performance energy storage materials, advancing the principles of green chemistry through waste valorization and sustainable material design.

Received 27th March 2025
Accepted 17th May 2025

DOI: 10.1039/d5ra02140e

rsc.li/rsc-advances

Open Access Article. Published on 23 May 2025. Downloaded on 2/7/2026 11:23:07 PM.
This article is licensed under a Creative Commons Attribution-NonCommercial 3.0 Unported Licence.

1 Introduction

Supercapacitors have attracted much interest in recent years because they exhibit high power density, short charge–discharge times, and long cycle life.[1–3] These characteristics make them suitable for several different applications for example portable electronics,[4] electric vehicles,[5] and renewable energy storage systems.[6] Nonetheless, the advancement of new materials used in electrodes is one of the major issues to be solved since energy density poses a significant problem for supercapacitors when compared to conventional batteries.[7–9]

The exploration of biomass-derived materials for supercapacitor electrodes has gained importance as a strategy to address environmental issues caused by biomass waste.[10] Converting waste into valuable products aligns with the principle of "turning trash into treasure".[11] Carbon material derived from waste biomass is a valuable product.[12] However, achieving high-performance carbon-based materials from natural resources or industrial waste with high efficiency remains a significant challenge.[13–15]

Two-dimensional (2D) carbon materials are promising for next-generation supercapacitors and as precursors for three-dimensional (3D) porous carbon aerogels due to their high surface area, lightweight nature, and excellent electrolyte accessibility, which enhances rate performance and specific capacitance.[16–18] However, commercial production of 2D carbon materials, typically through the exfoliation of graphite oxide, is often complex, costly, and inefficient.[19] Using waste biomass to prepare 2D porous carbon is an attractive alternative.[15] For example, carbon nanosheets from hemp demonstrated ultrafast electrochemical storage and good capacitance retention, while N-doped porous carbon sheets from eggplants showed high-rate performance.[20] Despite these advancements, the specific capacitance of such materials (100–150 F g^{-1}) remains lower than that of activated carbon. In contrast, large porous carbon nanosheets derived from gelatin exhibited a specific capacitance of 246 F g^{-1} and excellent retention.[21] Selecting appropriate biomass precursors is an effective strategy for creating high-performance 2D porous carbon materials for supercapacitors.

Water hyacinth, a rapidly growing and abundant aquatic plant found in tropical and subtropical regions, is gaining attention for its cost-effectiveness and availability.[22] Porous carbon derived from water hyacinth exhibits favorable electrochemical performances, including high specific capacitance and favorable cycling stability. These characteristics are mainly attributed to the specific microstructure involving cellulose fiber network and air pockets for the to and fro movement of ions and large surface area for more storages that summarize the capacitance and energy density of the supercapacitors.[20,23,24] Furthermore, one can also find that water hyacinth fibers possess high electrical conductivity that would help in the charge transfer between the electrode and the electrolyte.

Department of Chemistry, CHRIST University, Bengaluru 560029, India. E-mail: sreeja.pb@christuniversity.in

† Electronic supplementary information (ESI) available. See DOI: https://doi.org/10.1039/d5ra02140e

© 2025 The Author(s). Published by the Royal Society of Chemistry

Open Access Article. Published on 23 May 2025. Downloaded on 2/7/2026 11:23:07 PM.
This article is licensed under a Creative Commons Attribution-NonCommercial 3.0 Unported Licence.

Polypyrrole is a conductive polymer that has been identified as a candidate material for an electrode because of its high theoretical specific capacitance and a good electrical conductivity especially when mixed with activated carbon from water hyacinths.[25–28] However, the material face some difficulties related to cycling stability of PPy when used in the long term; this may limit its application. Some of the recent studies include the use of transition metal oxides and carbon as additives for the assessment of changes in the impedance profile and cycling stability of high surface area electrode materials. However, the material face some difficulties related to cycling stability of PPy when used in the long term; this may limit its application. Some of the recent studies include the use of transition metal oxides and carbon as additives for the assessment of changes in the impedance profile and cycling stability of high surface area electrode materials.[14,15,28]

To overcome such limitations and enhance the integration of PPy with other components, interfacial polymerization is employed as a synthetic strategy. In this process, pyrrole monomers are oxidatively polymerized at the interface of the aqueous dispersion of metal oxides and carbon precursors, typically in the presence of an oxidizing agent ($FeCl_3$).[25,29] This method facilitates the uniform coating of PPy over the substrate surface, forming a conductive and electrochemically active layer.[30] The controlled growth at the interface ensures better contact and adhesion between the components, thereby improving electron transport and mechanical stability during cycling.

Among these metal oxides, titanium dioxide (TiO_2 or titania) is recognized to possess highest positive charge (Ti^{4+}) thus can have superior electron donor sites for the interaction.[31] The anatase form of titania is preferred for its longer charge-carrier recombination time and higher surface area.[32–35] The addition of conducting polymers like PPy together with metal oxides and carbon-based materials also enhance electrode characteristics by delivering high energy density as well as favourable capacitance values.

This study outlines a systematic approach for creating a novel water hyacinth–titanium dioxide/polypyrrole composite by integrating PPy onto TiO_2 composited with WH for use as an electrode material in supercapacitors. The composite was synthesized by initially combining TiO_2 with water hyacinth-derived carbon, followed by grafting PPy through interfacial polymerization. The electrochemical analysis of the WH–TiO_2/PPy composite demonstrated enhanced performance due to the synergistic interaction of its components. An asymmetric supercapacitor was constructed using the WH–TiO_2/PPy. The results showed a significant improvement in cycling stability, which is attributed to the WH-derived carbon matrix acting as a buffer between TiO_2 and PPy, preventing nanosheet agglomeration, increasing surface area, and improving electrolyte ion penetration. This research supports the development of sustainable and high-performance supercapacitor electrodes, contributing to advancements in energy storage technology.

2 Experimental techniques

2.1 Materials

The pyrrole monomer, titanium dioxide, 85.0% potassium hydroxide (KOH), hydrochloric acid (HCl), ethanol, ammonium persulfate (APS), *N*-methyl-2-pyrrolidone (NMP), polyvinylidene fluoride (PVDF), activated carbon and carbon black were all procured from Sigma-Aldrich and utilized as received without any additional purification steps. Moreover, water hyacinth was gathered from a canal located near the residential area of the southern part of India.

2.2 Raw material preparation

WH was collected from local stagnant water bodies in Nileshwar, Kerala. The collected WH was cut into small pieces, thoroughly cleaned with deionized water (DI), and then dried in an oven at 80 °C for an extended period. Once dried, the WH was ground into a fine powder using a grinder. To remove lignin, the powdered WH was treated with a 15% KOH solution and left to soak for 24 h. After delignification, the treated WH powder was separated from the solution by centrifugation and filtration and then washed multiple times with distilled water (until the pH was ~7).

The washed powder was then subjected to pyrolysis in a muffle furnace under an oxygen-free environment. The temperature was first raised to 400 °C and maintained for 1 h, then increased to 600 °C for an additional h and finally brought to 800 °C for 1.5 h. After pyrolysis, the resulting black powder was washed several times with a 1 M HCl solution in DI water to remove any remaining inorganic impurities and was subsequently dried in air.[36]

2.3 Synthesis of WH–TiO_2/PPy

The WH–TiO_2/PPy composite is synthesized through a two-step process involving an initial hydrothermal treatment[37] followed by interfacial polymerization.[25] The prepared WH powder was mixed with TiO_2 and ultrasonicated in 1 M HCl solution for 1 h to ensure uniform dispersion and facilitate surface activation of the components prior to further processing. The WH–TiO_2 mixture was subjected to heat treatment at 180 °C for 10 hours to strengthen the connection between the components and optimize the properties of the final composite. In a separate step, pyrrole monomer was dissolved in a 1.0 mol per L HCl solution. Both the WH–TiO_2 mixture and the pyrrole solution were transferred to a 1-litre beaker placed in an ice bath on a magnetic stirrer. A 0.125 mol per L APS solution was slowly added to the mixture using a burette while maintaining constant mechanical stirring at a temperature of 0–5 °C for 1 hour. This step initiates the interfacial oxidative polymerization of pyrrole, where APS acts as the oxidizing agent to polymerize pyrrole monomers adsorbed onto the surface of WH–TiO_2. This controlled interfacial polymerization facilitates the uniform formation of the PPy layer on the TiO_2 surface, enhancing interfacial contact, improving electron transport, and contributing to mechanical stability during charge/discharge cycles. The mixture was then stirred continuously for an additional 24

Open Access Article. Published on 23 May 2025. Downloaded on 2/7/2026 11:23:07 PM. This article is licensed under a Creative Commons Attribution-NonCommercial 3.0 Unported Licence.

hours at the same temperature (0–5 °C). Upon completion, the resulting suspension was filtered and washed multiple times with distilled water and ethanol to remove any unreacted materials. The filtered product was then dried at 60 °C and labelled as WH–TiO_2/PPy. The synthesis process is illustrated in Fig. 1.

2.4 Characterization

The surface morphology and distribution of WH–TiO_2/PPy were analysed using Scanning Electron Microscopy equipped with energy-dispersive X-ray spectroscopy (SEM-EDX, Nova 450). To examine the structure of the materials, Transmission Electron Microscopy (TEM, JEM-2100 HRTEM) was employed, specifically focusing on the WH–TiO_2/PPy within the sample. An X-ray diffractometer (XRD, Rigaku D/max 2500PC) was employed to confirm the presence of WH–TiO_2/PPy in the materials. The functional groups within the composite were identified using Fourier transform infrared (FTIR) spectrometry with a single-reflectance ATR accessory (Shimadzu IR spirit). Additionally, X-ray photoelectron spectroscopy (XPS, K-Alpha spectrometer KAN9954133) was used to analyze the surface functional groups and elemental composition of the materials.

2.5 Electrochemical characterisation and preparation

The preparation of the working electrode involved two key steps. First, nickel foam was cut into pieces measuring 1.5 cm × 1.0 cm. Samples were rinsed in acetone under ultrasonic treatment and then in a 0.1 M HCl solution in order to remove the surface nickel oxide.[38] The treated nickel foam was then vacuum-dried for further use. Next, a mixture of WH–TiO_2/PPy composite, carbon black, and PVDF in an 8 : 1 : 1 ratio was ground uniformly and thoroughly mixed with NMP solvent to form a slurry. This slurry was applied evenly onto a 1.0 cm × 1.0 cm section of the nickel foam. The coated electrode was packed in a tablet press at a pressure of 15 MPa and was vacuum dried for 12 hours before testing. The WH and WH/PPy composite was also synthesized in the same way so that there is uniformity in electrode synthesis.

The electrode loading was measured using an electronic balance with a precision of 0.01 mg. First, the weight of the Torrey paper was recorded, followed by the weight of the coated electrode after drying the ink on a 1 × 1 cm^2 section of Torrey carbon paper. The difference in weights was used to determine the precise electrode material loading, which typically totalled 3–5 mg of active material, carbon, and PVDF binder.[39]

The electrochemical performance of the prepared electrode was evaluated using a traditional three-electrode system. In this setup, a saturated Ag/AgCl (saturated KCl) electrode was used as the reference electrode, the working electrode consisted of nickel foam coated with the WH–TiO_2/PPy composite, and a platinum wire served as the counter electrode. Electrochemical measurements were conducted using an electrochemical workstation (CHI608E). The electrode materials were analyzed using cyclic voltammetry (CV), galvanostatic charge–discharge (GCD), and electrochemical impedance spectroscopy (EIS) in a 3 M KOH aqueous solution at room temperature. The potential windows for CV and GCD tests were set between −0.4 to 0.6 V. At different scan rates ranging from 5 to 100 mV s^{-1}. GCD analysis was conducted at current densities ranging from 1 to 5 Ag^{-1}. Eqn (1)[40] were utilized to determine the gravimetric capacitance (C).

$$C = \frac{I \times \Delta t}{m \times \Delta v} \quad (1)$$

In eqn (1), C (Fg^{-1}) represents the gravimetric capacitance, with I (A) denoting the discharge current in a unit of A g^{-1}, Δt (s) representing the discharge duration, and ΔV (V) indicating the

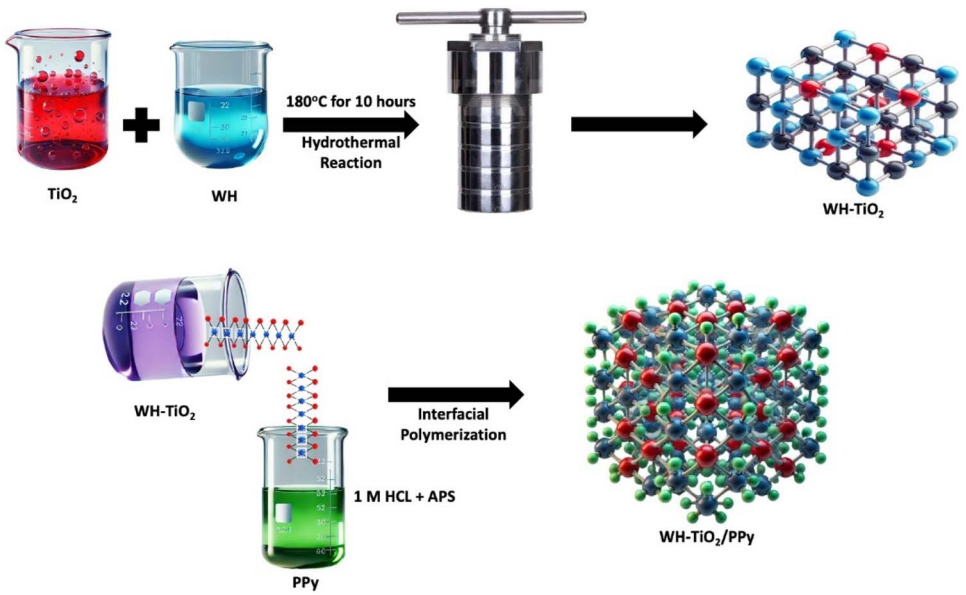

Fig. 1 Schematic illustration of the preparation process of WH–TiO_2/PPy.

© 2025 The Author(s). Published by the Royal Society of Chemistry

Open Access Article. Published on 23 May 2025. Downloaded on 2/7/2026 11:23:07 PM.
This article is licensed under a Creative Commons Attribution-NonCommercial 3.0 Unported Licence.

potential shift during that duration Δt (s). The weight of active material is given by m (g).

2.6 Asymmetric supercapacitor and testing

An asymmetric supercapacitor was assembled using WH–TiO_2/PPy as the positive electrode, activated carbon (AC) as the negative electrode, and 3 M KOH (in filter paper) as the separator. To optimize the electrochemical performance, the positive and negative electrodes need to maintain charge balance, where $q^+ = q^-(q = C \times m \times \Delta V)$. Thus, the optimal mass ratio of the two electrodes must meet the following equation:[41]

$$\frac{m_+}{m_-} = \frac{c_- \times \Delta v_-}{c_- \times \Delta v_+} \quad (2)$$

The electrochemical performance of the asymmetric supercapacitors was evaluated using a two-electrode system in a 3 M KOH electrolyte. The voltage window for both the cyclic voltammetry and galvanostatic charge–discharge tests was set from 0 to 1.6 V. The gravimetric capacitance of the asymmetric supercapacitor was determined using eqn (1). Subsequently, the gravimetric energy density (ED) and power density (PD) of the device were computed using the following eqn (3) & (4).[42]

$$\mathrm{ED} = \frac{C\Delta v^2}{2 \times 3.6} \quad (3)$$

$$\mathrm{PD} = \frac{\mathrm{ED}}{\Delta t} \times 3600 \quad (4)$$

Here, ED denotes the energy density, measured in watt-hours per kilogram (W h kg^{-1}), while PD represents the power density, measured in watts per kilogram (W kg^{-1}).

3 Results and discussion

3.1 Physical characterization

Fig. 2(a) displays the IR spectra of the WH, WH/PPy, and WH–TiO_2/PPy composites. The spectrum for WH shows a broad peak around 3145 cm^{-1}, which corresponds to O–H stretching vibrations,[43] typical of hydroxyl groups present in cellulose, hemicellulose, and lignin. A shoulder peak at 2967 cm^{-1} is attributed to C–H stretching in aliphatic chains, indicating the presence of carbohydrates.[44–46] The peak at 1607 cm^{-1} is associated with C=C stretching in aromatic rings,[47] suggesting lignin content and the peak at 1050 cm^{-1} corresponds to C–O stretching vibrations,[48] which is indicative of polysaccharides in the biomass. In the IR spectrum of the WH/PPy composite, new peaks are observed at 1520 and 1200 cm^{-1}, which are attributed to C=C stretching in the polypyrrole ring and C–N stretching vibrations, respectively.[49] These findings confirm the presence of polypyrrole in the composite. Furthermore, shifts and changes in the intensity of the O–H and C–O peaks suggest interactions between the water hyacinth and polypyrrole components.

For the WH–TiO_2/PPy composite, additional spectral changes are evident, a peak at 1767 cm^{-1} suggests C=O stretching vibrations, indicating oxidation due to the incorporation of TiO_2. Another new peak at 455 cm^{-1} is associated with Ti–O stretching vibrations, confirming the presence of TiO_2 in the composite, and additionally, O–Ti–O bending vibrations are observed within a similar spectral range.[50] These spectral changes highlight the successful integration of polypyrrole and TiO_2 into the WH matrix, which is consistent with the SEM results.

XRD patterns of WH, WH/PPy, and WH–TiO_2/PPy composites are shown in Fig. 2(b). For pristine WH, two broad peaks are observed at approximately 26° and 40°, corresponding to the (002) and (100) planes of turbostratic carbon,[51] respectively. These peaks indicate the presence of a disordered, graphene-like structure. The presence of the (100) peak suggests slight graphitization, which may enhance electrical conductivity. In the WH/PPy composite, the XRD pattern shows a broad peak around the range typically associated with polypyrrole. A distinct peak corresponding to the (110) phase of polypyrrole is observed, indicating the successful incorporation of polypyrrole into the WH matrix.[43] This incorporation results into a reduction of crystallinity which could improve the conductivity of the composite since polypyrrole possesses conjugated structure.

The XRD pattern of the WH–TiO_2/PPy composite shows several distinct peaks, including those corresponding to the (110) phase of polypyrrole and the (004), (200), (105), (211),

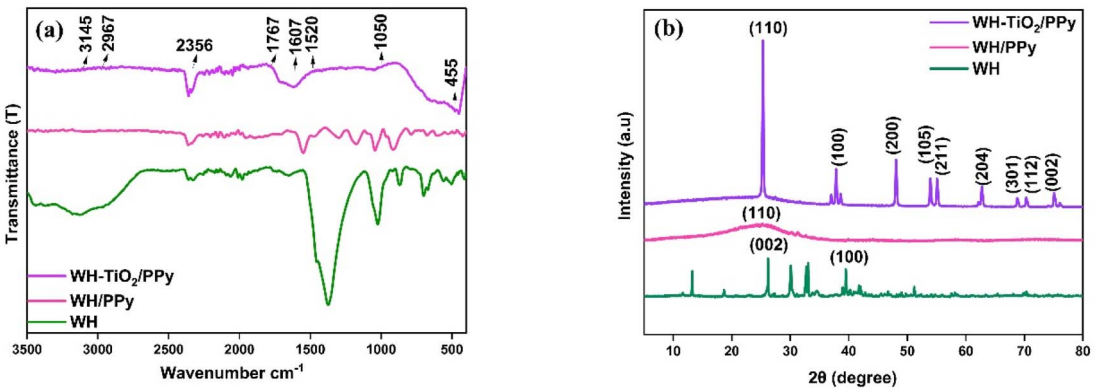

Fig. 2 (a) FTIR spectra of WH–TiO_2/PPy, WH/PPy, and WH, and (b) XRD patterns of WH–TiO_2/PPy, WH/PPy, and WH.

Open Access Article. Published on 23 May 2025. Downloaded on 2/7/2026 11:23:07 PM.
This article is licensed under a Creative Commons Attribution-NonCommercial 3.0 Unported Licence.

(204), (301), (112), and (002) planes of anatase TiO_2.[52] These peaks confirm the successful incorporation of both polypyrrole and TiO_2 into the composite. The sharp and well-defined peaks of TiO_2 indicate a crystalline structure, which may contribute to enhanced mechanical strength and electrochemical activity. In the ternary WH–TiO_2/PPy composite, the original broad peaks associated with turbostratic carbon planes become less prominent or are completely obscured. This reduction in intensity or disappearance is due to the strong diffraction peaks of TiO_2 and the overlap with polypyrrole peaks, suggesting that the structural characteristics of water hyacinth are masked or significantly altered upon the incorporation of polypyrrole and TiO_2, forming a new composite material with modified properties.

SEM imaging was employed to investigate the microstructure and surface morphology of the samples, as shown in Fig. 3(a–f) at 500 nm and 1 μm. This indicates that all samples are composed of microspheres formed by numerous interconnected nanoparticles, though the specific structural details differ. Fig. 3(a and b) depicts the WH material, highlighting its layered, fibrous structure, which suggests a high surface area that can improve ion transport efficiency. The WH fibers display a sheet-like porous structure with irregular shapes and diameters, mainly composed of carbon and oxygen, along with smaller amounts of nitrogen, chlorine, sulfur, and potassium (Fig. S2†). Optimizing the pore size distribution is essential, particularly for supercapacitor electrodes, due to the material's high carbon content. The pyrolysis process in the muffle furnace created a combination of mesopores and micropores, resulting in a range of pore sizes and shapes (Fig. S3†).

Fig. 3(c and d) display SEM images of the WH/PPy composite material. These images show the formation of uniform microspheres consisting of PPy particles that are evenly distributed throughout the WH structure. The spherical shape of the particles indicates that PPy is well integrated into the WH matrix, forming a porous structure with interconnected networks. This even distribution and integration of PPy

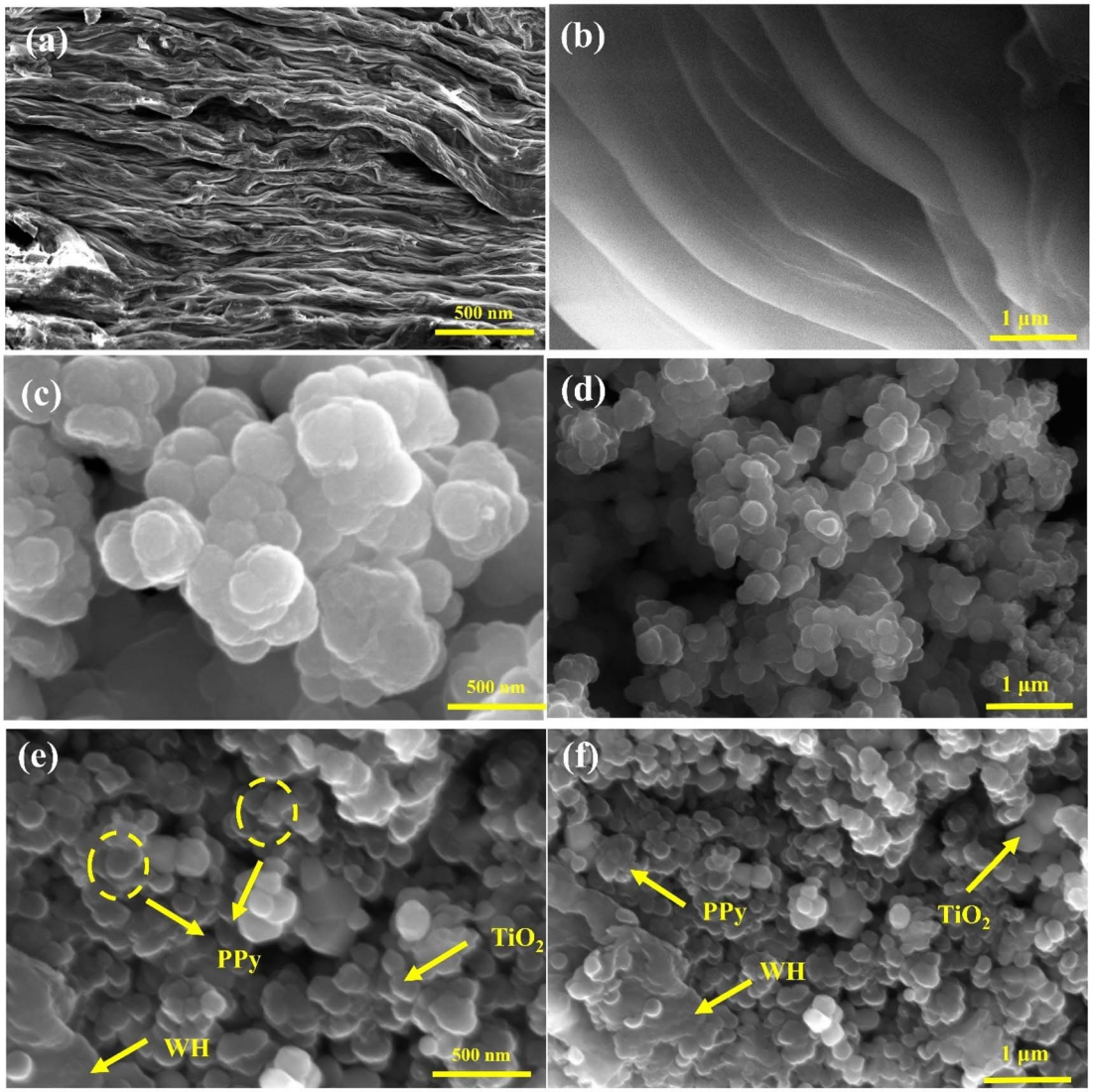

Fig. 3 SEM images of (a and b) WH, (c and d) WH/PPy and (e and f) WH–TiO_2/PPy composites.

© 2025 The Author(s). Published by the Royal Society of Chemistry

Open Access Article. Published on 23 May 2025. Downloaded on 2/7/2026 11:23:07 PM. This article is licensed under a Creative Commons Attribution-NonCommercial 3.0 Unported Licence.

enhance the overall conductivity of the composite and increase its surface area. The microstructure observed in these images suggests that WH acts as an effective base for the polymerization of PPy, leading to the creation of a strong and conductive composite material.

The SEM image of the WH–TiO_2/PPy composite showed irregular spherical morphology as evident from Fig. 3(e and f) due to successful PPy polymerization on the presented WH–TiO_2 nanosheets. This combination is indicative of strong interfacial bonding among the components, which is expected to improve the overall electrochemical performance of the composite. The TiO_2 nanoparticles are uniformly distributed across the surface, while PPy particles are seen adhering to both the WH fibers and TiO_2, forming a cohesive structure. The interconnected network of WH provides a porous scaffold, facilitating better ion transport and contributing to a larger surface area, while the uniform dispersion of TiO_2 and PPy enhances conductivity and structural stability. The formation of PPy between individual layers of WH–TiO_2 was highlighted in the image with a dotted circle.

TEM images provided the morphology, crystallinity, and phase composition of a composite material. In Fig. 4(a and b) images, taken at 50 nm and 100 nm magnifications, spherical particles can be observed with varying sizes, indicating a polydisperse nature. These particles are likely aggregates of smaller nanoparticles, which can be seen more clearly in the higher magnification image in Fig. 4(b). The uniform and dense appearance of these aggregates suggests good connectivity between the particles, which is beneficial for the mechanical stability and functional properties of the composite.

Fig. 4(c) HRTEM, showing lattice fringes within the nanoparticles. The presence of these fringes indicates crystalline regions within the nanoparticles. The measured lattice spacings are approximately 0.22 and 0.35 nm, with the 0.22 nm spacing corresponding to the (110) plane of PPy[53] and the 0.35 nm spacing matching the (200) plane of anatase TiO_2.[54] These measurements confirm the presence of anatase TiO_2 in the composite, aligning with the XRD results in the WH–TiO_2/PPy composite.

Fig. 4(d) presents the SAED pattern of the synthesized composite, displaying distinct diffraction rings that demonstrate the crystalline nature of the material. The diffraction rings are indexed to the (110), (004), (200), (105), and (204) planes (JCPDS no. 21-1272),[55] which are characteristic of the anatase phase of TiO_2, a crystalline form widely recognized for its strong electrochemical properties. The presence of the (110) plane is also notable, as it indicates the successful incorporation of PPy within the composite. This confirms that the TiO_2 nanoparticles are effectively integrated into the PPy, forming a hybrid material. In addition, the WH component contributes as a carbon-based matrix that interacts with both PPy and TiO_2, forming a hybrid structure.

The anatase TiO_2 phase, particularly along the (004) and (200) planes, is known to improve electrochemical performance by offering active sites for charge storage and efficient ion transport.[56] The conductive PPy enhances charge transfer and mechanical flexibility, while the WH component, acting as a carbon-based matrix, interacts with both PPy and TiO_2, forming a hybrid structure. This combination improves cycling stability and charge–discharge performance. The diffraction rings in Fig. 4(d) confirm the presence of a well-crystallized composite, consistent with XRD and HRTEM observations, supporting its potential for high-performance supercapacitors.

XPS analysis was conducted to investigate the surface chemical composition and electronic states of the WH–TiO2/PPy composite. The survey spectrum (Fig. 5(a)) provides an overview, while high-resolution XPS spectra for Ti 2p, C 1s, N 1s, and O 1s regions (Fig. 5b–e) offer detailed insights into the binding behavior of the elements in the ternary polymer composite.

The high-resolution C 1s spectrum in Fig. 5(b) reveals: a peak at 284.23 eV, corresponding to graphitic carbon (sp^2), indicating the presence of a graphitic structure; a peak at 285.13 eV, attributed to C–C (sp^3) bonds, which signifies aliphatic carbon; and additional peaks at 286.18 eV and 288.09 eV, assigned to C–N/C–O and C=O functional groups, respectively.[57] These oxygen- and nitrogen-containing functional groups indicate successful material functionalization, which could enhance electrochemical performance.

The N 1s spectrum in Fig. 5(c) was deconvoluted into four peaks: 398.33 eV, corresponding to pyridinic-N, which contributes to pseudocapacitance; 399.63 eV and 400.48 eV, assigned to pyrrolic-N and graphitic-N, respectively,[53] which improve electronic conductivity; and 401.02 eV, representing oxidized nitrogen species, potentially contributing to redox reactions in supercapacitor electrodes. In the O 1s spectrum in Fig. 5(d), three distinct peaks were observed: 531.28 eV, associated with Ti–O bonds, indicating the successful incorporation of titanium into the composite; 532.53 eV, attributed to C–O groups; and 533.18 eV, corresponding to C=O groups.[58] These oxygenated groups can improve hydrophilicity and enhance pseudocapacitance through redox reactions.

In Fig. 5(e) Ti 2p spectrum was deconvoluted into Ti $2p_{3/2}$ and Ti $2p_{1/2}$ peaks at 459.18 eV and 464.68 eV, respectively,[59] confirming the presence of titanium in the Ti(IV) oxidation state, indicating titanium exists as TiO_2 in the composite, which contributes to capacitance through pseudocapacitive properties. These deconvoluted results align well with previously reported studies, further confirming the successful incorporation of PPy, WH, and TiO_2 in the ternary WH–TiO_2/PPy composite.

3.2 Electrochemical characterization

The CV curves presented in Fig. 6(a) illustrate the electrochemical performance of WH–TiO_2/PPy, WH/PPy, and WH-based electrodes at a scan rate of 100 mV s^{-1} with a potential range of −0.4 to 0.6 V. Among the three, the WH–TiO_2/PPy electrode demonstrates the highest current density, indicating superior electrochemical performance. This result suggests that the combination of WH, TiO_2, and polypyrrole significantly enhances charge storage, likely due to improved electrical conductivity, increased surface area, and the added pseudocapacitance from TiO_2 and PPy.[60] Fig. 6(b) shows the CV profiles of the WH electrode at various scan rates (5–100 mV s^{-1}), with

Open Access Article. Published on 23 May 2025. Downloaded on 2/7/2026 11:23:07 PM.
This article is licensed under a Creative Commons Attribution-NonCommercial 3.0 Unported Licence.

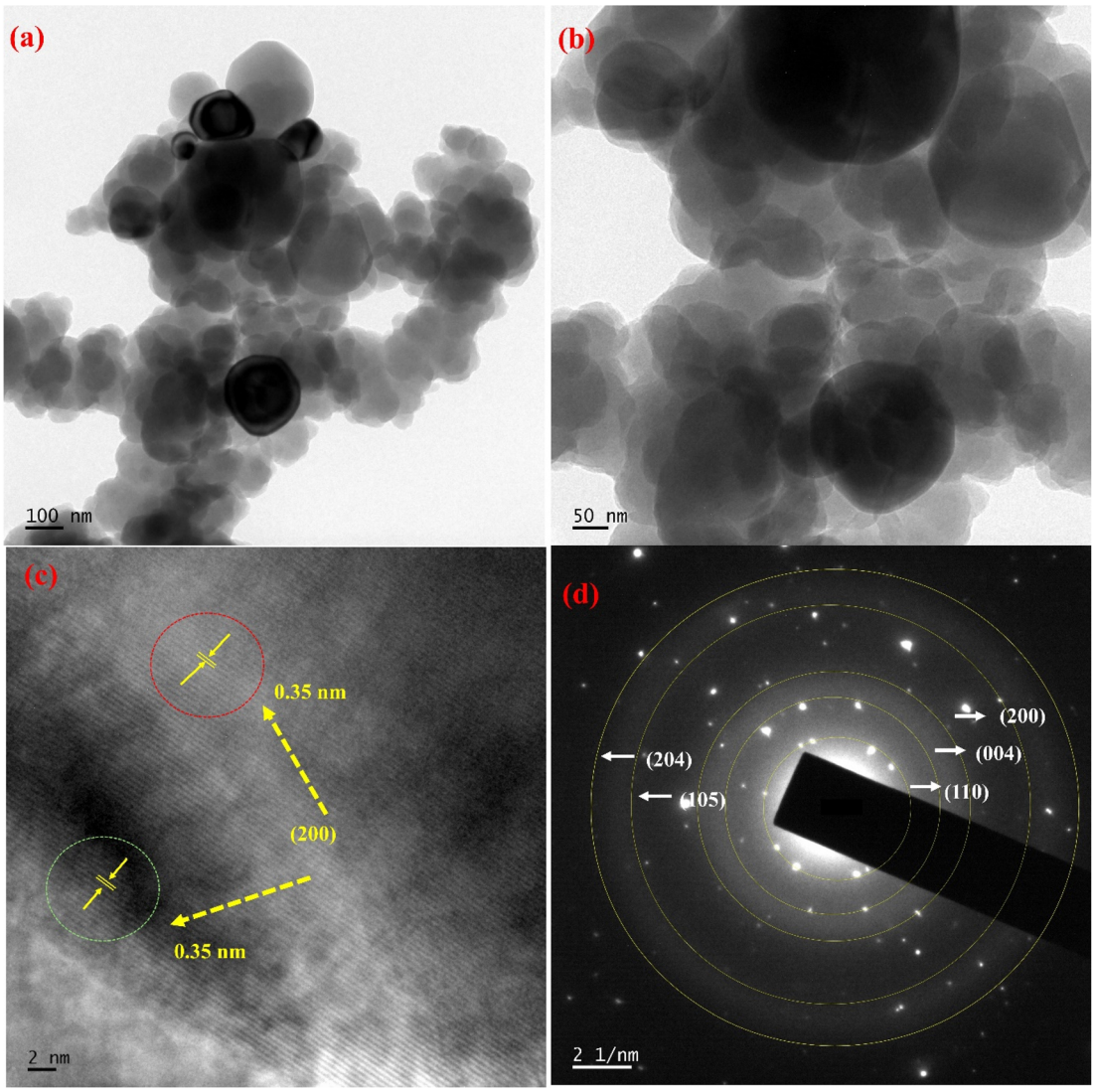

Fig. 4 TEM images showing the morphology of WH–TiO_2/PPy at (a) 50, (b) 100 nm, (c) HRTEM, (d) SAED pattern.

nearly no redox peaks suggesting stable capacitive behavior across different scan rates. WH alone exhibits basic capacitive behavior, however, the current densities for WH are considerably lower than those of the other electrodes, indicating a lack of pseudocapacitive contribution compared to the TiO_2 and PPy composites.

Fig. 6(c) and (d) display the CV profiles for WH/PPy and WH–TiO_2/PPy composites, respectively, at different scan rates. Both electrodes exhibit clear redox peaks, indicating pseudocapacitance due to polypyrrole. The WH–TiO_2/PPy composite shows significantly higher current densities across all scan rates, demonstrating superior charge storage compared to WH/PPy. These curves exhibited non-linearity, consistent with the presence of redox peaks observed in CV curves, indicating a pseudocapacitive behavior with changes in slope over time, indicative of cation insertion/extraction from the KOH electrolyte.[39] The inclusion of TiO_2 enhances the performance of the WH/PPy matrix by increasing the surface area and facilitating faster charge transfer. As scan rates increase, the redox peaks shift slightly, which is typical for pseudocapacitive materials. This makes the WH–TiO_2/PPy composite a more promising candidate for supercapacitor applications, owing to its enhanced charge storage and energy performance compared to the WH and WH/PPy counterparts.

This reveals a clearer relationship between discharge time and current density for the WH–TiO_2/PPy composite, as demonstrated in the GCD curves shown in Fig. 7(a). At current densities below 0.5 A g^{-1}, longer discharge times correspond to lower current densities, and *vice versa*. This suggests that the WH–TiO_2/PPy electrode exhibits enhanced energy storage capacity, as its slower discharge process indicates higher charge retention. The reduction in discharge time at higher current densities, such as 0.75 and 1 A g^{-1}, is due to the decreased time available for ion diffusion and charge transfer, a common characteristic of materials designed for supercapacitors. This improved performance is primarily attributed to the integration

© 2025 The Author(s). Published by the Royal Society of Chemistry

Open Access Article. Published on 23 May 2025. Downloaded on 2/7/2026 11:23:07 PM.
This article is licensed under a Creative Commons Attribution-NonCommercial 3.0 Unported Licence.

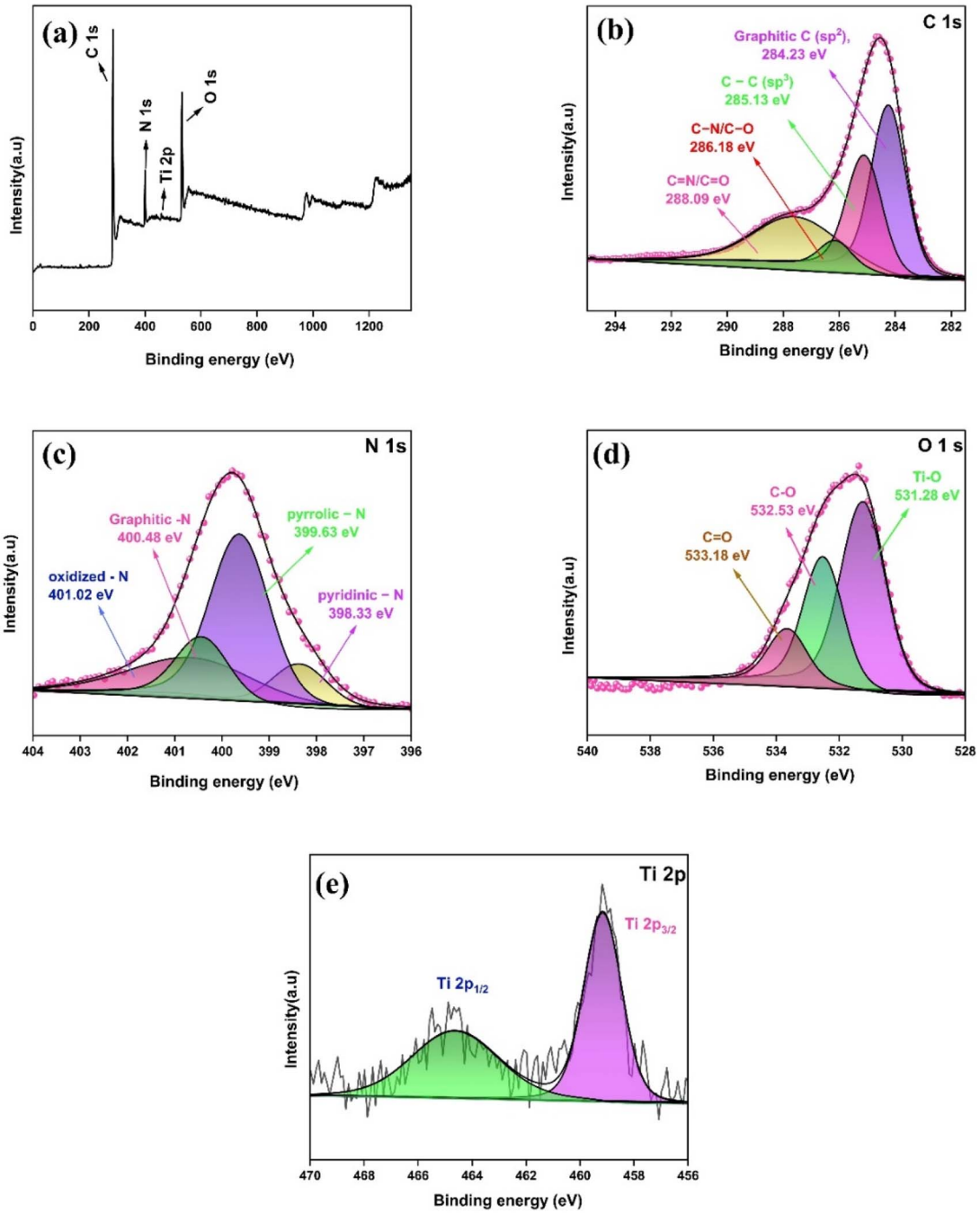

Fig. 5 XPS analysis of WH–TiO_2/PPy composite: (a) survey spectrum, (b) C 1s, (c) N 1s, (d) O 1s, (e) Ti 2p.

of TiO_2 and polypyrrole within the WH matrix. TiO_2 contributes high specific surface area and promotes electron transport, while PPy provides pseudocapacitance *via* reversible redox reactions. This synergistic effect renders WH–TiO_2/PPy superior to WH, as reflected by the significantly higher discharge times and current densities in the GCD curves. Table 1 compares various composite electrodes based on water hyacinth and polypyrrole.

Fig. 7(b) shows the gravimetric capacitance at different current densities for both WH–TiO_2/PPy and WH electrodes. The WH–TiO_2/PPy composite achieves a remarkable capacitance of 610 F g^{-1} at 0.5 A g^{-1}, 428 F g^{-1} at 0.75 A g^{-1}, and 285 F g^{-1} at 1 A g^{-1}, significantly outperforming the WH electrode at all current densities. This substantial improvement in capacitance can be attributed to the pseudocapacitive contribution and enhanced conductivity provided by PPy, along with the increased surface area offered by TiO_2. Similar trends have been observed in recent studies where the integration of metal oxides and conductive polymers into carbon-based matrices greatly enhanced the charge storage capacity and overall

Open Access Article. Published on 23 May 2025. Downloaded on 2/7/2026 11:23:07 PM.
This article is licensed under a Creative Commons Attribution-NonCommercial 3.0 Unported Licence.

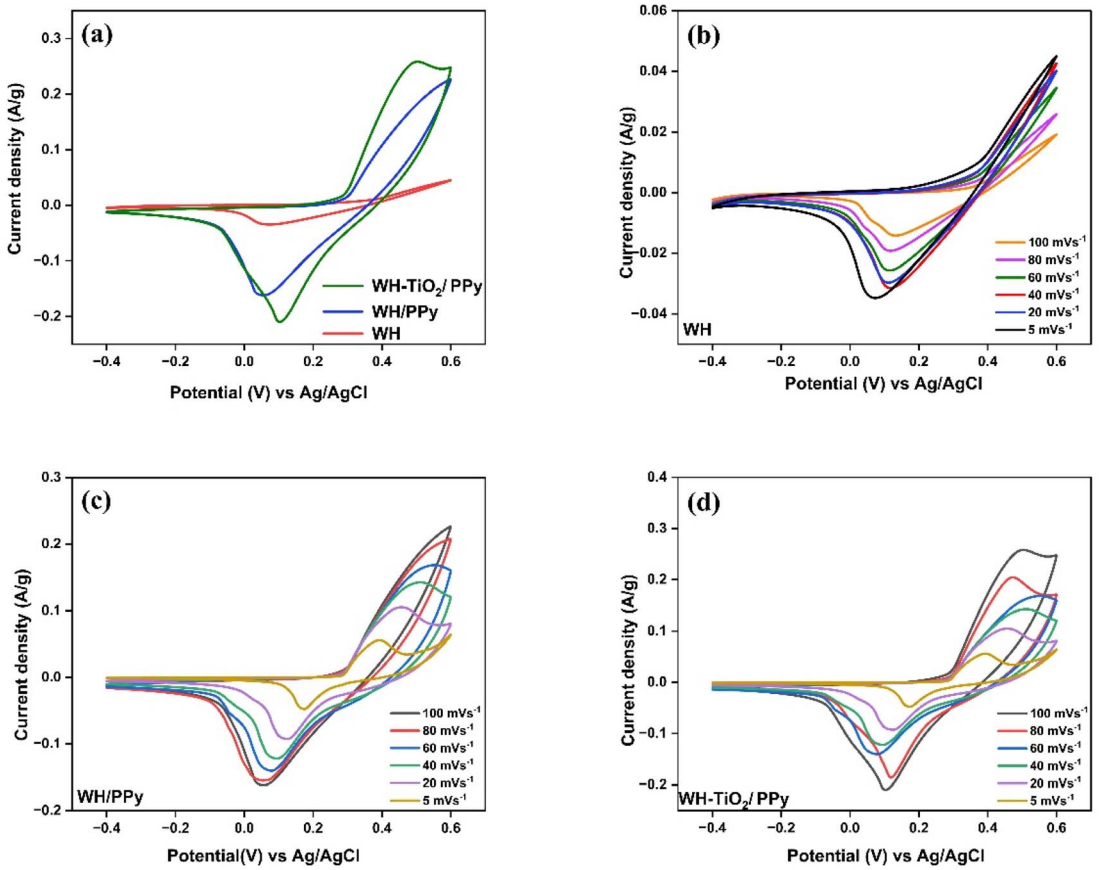

Fig. 6 (a) Cyclic voltammograms of WH, WH/PPy, and WH–TiO_2/PPy electrodes in 3 M KOH electrolyte at a constant sweep rate of 100 mV s^{-1}. Comparison of CV profiles for (b) WH, (c) WH/PPy, and (d) WH–TiO_2/PPy at a scan rate (5–100 mV s^{-1}).

performance.[67] Although the capacitance decreases as the current density increases, which is typical of pseudocapacitive materials due to limited ion diffusion at higher rates, the performance of the WH–TiO_2/PPy composite remains significantly higher than that of WH alone.

EIS is a valuable technique for studying the electrical properties of electrodes in electrolytes over a frequency range of 0.01–100 kHz. Nyquist plots typically feature a semicircle in the high-frequency region and a straight line in the low-frequency region.[68] In the Nyquist plots of Fig. 7(c), the superior performance of the WH–TiO_2/PPy composite is evident. The charge transfer resistance (R_{ct}) of the ternary composite (0.63 Ω) is significantly lower than that of WH (1.31 Ω) alone. The smaller R_{ct} values indicate low faradaic resistance and fast electrochemical reactions at the electrode–electrolyte interface.[69] The low R_{ct} is attributed to the porous structure and good electrical conductivity of WH–TiO_2/PPy, facilitating better ion exchange in the 3 M KOH electrolyte. The size of cations in the electrolyte also plays a key role in determining charge-transfer resistance, with larger cations leading to higher R_{ct}. The Nyquist plot for WH–TiO_2/PPy shows a straight line in the low-frequency region, indicating the ideal capacitive behavior of the electrode.

Fig. 7(d) illustrates the cycling stability of the WH–TiO_2/PPy and WH electrodes over 5000 charge/discharge cycles at a current density of 5 A g^{-1}. The WH–TiO_2/PPy composite retains over 94% of its initial capacitance, demonstrating excellent cycling stability. In contrast, the WH electrode exhibits more significant degradation, retaining only around 69% of its capacitance after 5000 cycles. The outstanding cycling stability of the WH–TiO_2/PPy composite can be attributed to the strong integration of TiO_2 and PPy, which provides mechanical stability and prevents significant structural degradation during repeated cycling. Overall, the superior capacitance, lower charge transfer resistance, and excellent cycling stability of the WH–TiO_2/PPy composite make it a promising candidate for advanced supercapacitor applications.

3.3 Fabrication of WH–TiO_2/PPy//AC asymmetric supercapacitor

An asymmetric supercapacitor was fabricated using WH–TiO_2/PPy as the positive electrode and activated carbon as the negative electrode. Asymmetric supercapacitors with aqueous electrolytes are an effective method for enhancing both ED ana PD.[70] In this study, the asymmetric supercapacitor was assembled in a two-electrode configuration, with Whatman filter paper-2 soaked in 3 M KOH acting as the separator. Fig. 8 provides a schematic representation of the assembly process for the asymmetric supercapacitor device incorporating WH–TiO_2/PPy//AC electrodes.

© 2025 The Author(s). Published by the Royal Society of Chemistry

Open Access Article. Published on 23 May 2025. Downloaded on 2/7/2026 11:23:07 PM.
This article is licensed under a Creative Commons Attribution-NonCommercial 3.0 Unported Licence.

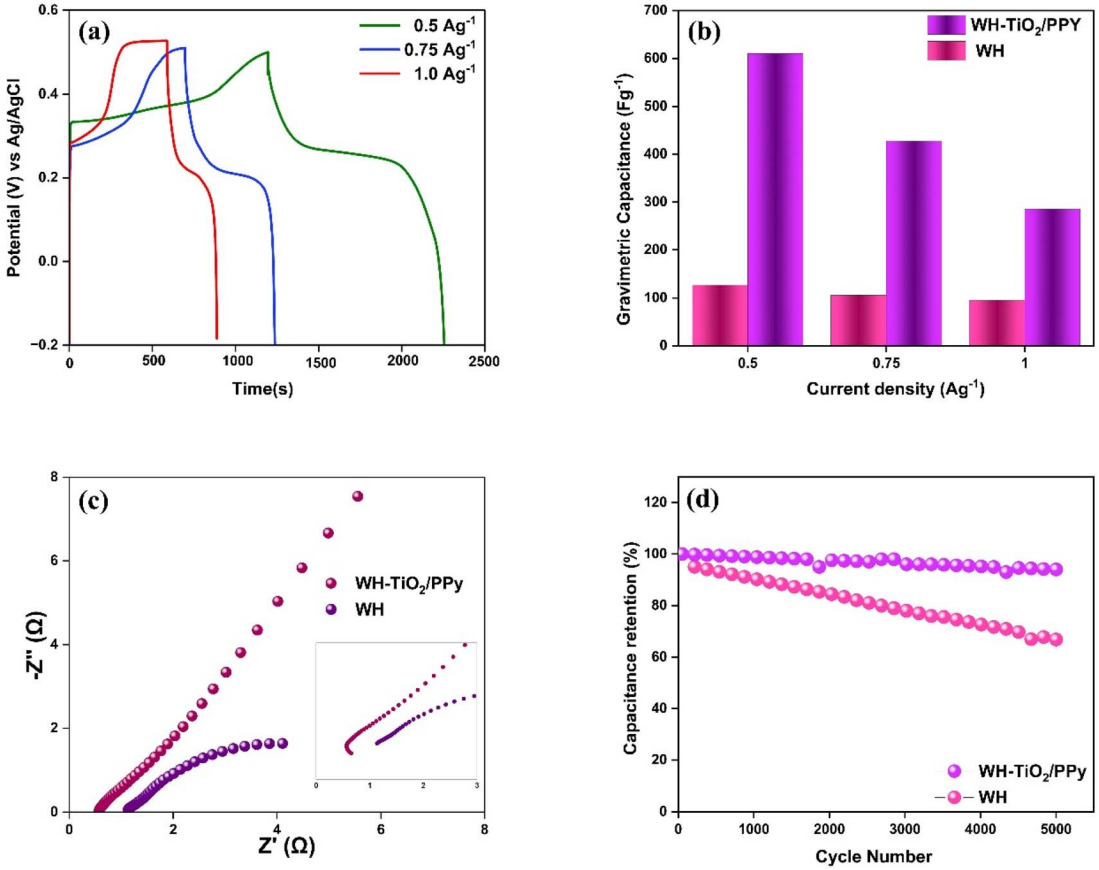

Fig. 7 (a) Galvanostatic charge–discharge curves of WH–TiO_2/PPy at different current densities, (b) gravimetric capacitance of WH–TiO_2/PPy and WH (c) Nyquist plots for WH–TiO_2/PPy and WH, (d) cycling stability of WH–TiO_2/PPy and WH.

To elucidate the charge storage mechanisms of WH–TiO_2/PPy in comparison to AC, two-electrode asymmetric supercapacitor measurements were performed in a 3 M KOH electrolyte. Fig. 9(a) shows CV curves at different scan rates, ranging from 5 to 100 mV s^{-1}, within a potential window of 0–1.6 V. The curves display a combination of pseudocapacitive EDLC behavior. Broad redox peaks at lower scan rates indicate faradaic reactions from the WH–TiO_2/PPy electrode, while the rectangular shape at higher scan rates suggests the EDLC contribution from the activated carbon electrode. As the scan rate increases, the current response grows with minimal distortion, demonstrating good charge storage properties and fast ion transport in the supercapacitor.

Fig. 9(b) presents charge–discharge curves used to measure the electrode capacitance, calculated using eqn (1). The WH–TiO_2/PPy//AC asymmetric supercapacitor shows capacitance

Table 1 The literature reports on the electrochemical performance of several WH-based composite electrodes

Material	Specific capacitance	Method	Capacitance retention	Cycles	Reference
Polypyrrole/water hyacinth	104 F g^{-1}	Polymerisation	67%	1500	44
Water hyacinth	98 F g^{-1}	Pyrolytic carbonization	84%	500	61
Carbon sheets derived from water hyacinth	273 F g^{-1}	Acid treatment, pyrolytic carbonization	99%	10 000	62
Water hyacinth-derived carbon	344 F g^{-1}	Pre-carbonization and KOH activation	95%	10 000	63
WH/$Ni2^{+}$ biomass from the phytoremediation of Ni_2O	541 F g^{-1}	Phytoremediation	100%	10 000	64
Water hyacinth-derived activated carbon/NiO	249 F g^{-1}	Electrochemical deposition	78.5%	1000	65
PEDOT/water hyacinth	490 F g^{-1}	Polymerisation	92%	2000	66
Water hyacinth-derived activated carbon, polypyrrole, and titanium dioxide	610 F g^{-1}	Hydrothermal & interfacial polymerisation	94%	5000	This work

Open Access Article. Published on 23 May 2025. Downloaded on 2/7/2026 11:23:07 PM.
This article is licensed under a Creative Commons Attribution-NonCommercial 3.0 Unported Licence.

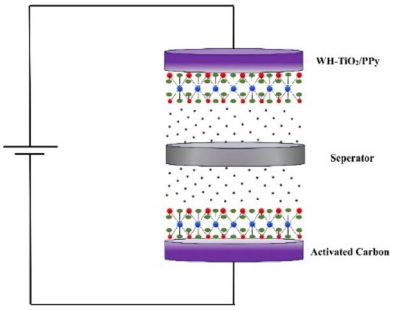

Fig. 8 The schematic assembly process for the asymmetric supercapacitor of WH–TiO_2/PPy//AC.

values of 262 F g^{-1} at current densities of 1 A g^{-1}. The nearly linear discharge profiles indicate excellent capacitive behavior and low internal resistance. Longer discharge times at lower current densities suggest a higher energy storage capacity under these conditions.

Fig. 9(c) depicts the EIS plot (Nyquist) within the frequency range of 10 Hz to 10 kHz, confirming the superior charge transfer and capacitance of the WH-TiO_2/PPy//AC supercapacitor. The small semicircle in the high-frequency region of the Nyquist plot indicates a low charge transfer resistance of 0.84 Ω, highlighting efficient electron transfer at the electrode–electrolyte interface. The nearly vertical line in the low-frequency region signifies strong capacitive behavior and effective ion diffusion, confirming the high conductivity and excellent electrochemical performance of the WH–TiO_2/PPy//AC system. Fig. 9(d) illustrates the cycling stability of the supercapacitor over 5000 cycles, with the device retaining more than 80% of its initial capacitance, demonstrating its excellent durability and long-term stability. This performance is attributed to the robust integration of the WH–TiO_2/PPy composite, which maintains structural integrity and consistent electrochemical performance through repeated charge–discharge cycles.

Fig. 10(a) presents the gravimetric capacitance values of the WH–TiO_2/PPy//AC asymmetric supercapacitor as a function of current density. The WH–TiO_2/PPy//AC asymmetric supercapacitor shows capacitance values of 262, 243, 215, and 113 F g^{-1} at current densities of 1, 1.5, 2, and 2.5 A g^{-1}, respectively. This decrease in capacitance with increasing current density is attributed to insufficient ion diffusion at higher current densities, limiting access to active electrode sites. The relatively high capacitance at lower current densities suggests efficient charge

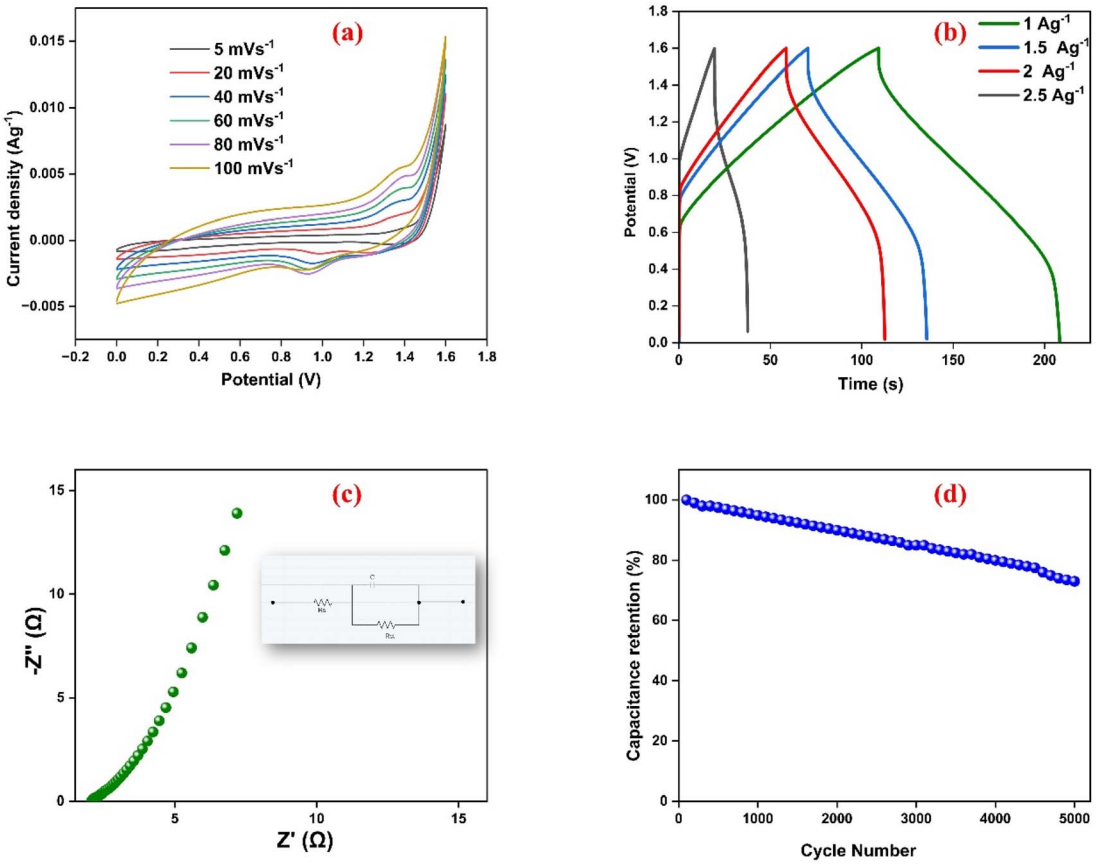

Fig. 9 Electrochemical performance of the WH–TiO_2/PPy//AC asymmetric supercapacitor in 3 M KOH electrolyte. (a) Cyclic voltammetry profiles at various scan rates, (b) galvanostatic charge–discharge curves recorded at different current densities, (c) Nyquist plot showcasing the impedance characteristics of the fabricated cell, and (d) cycling stability illustrating the capacitance retention over repeated charge–discharge cycles.

© 2025 The Author(s). Published by the Royal Society of Chemistry

Open Access Article. Published on 23 May 2025. Downloaded on 2/7/2026 11:23:07 PM.
This article is licensed under a Creative Commons Attribution-NonCommercial 3.0 Unported Licence.

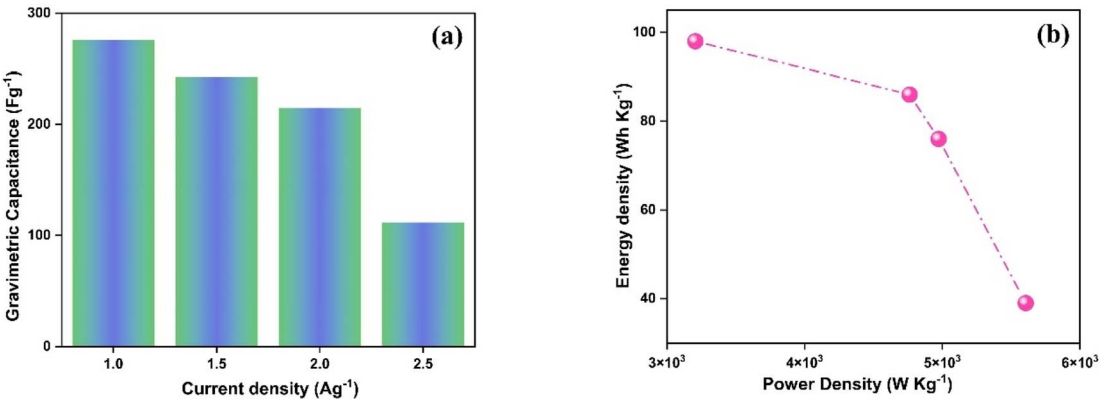

Fig. 10 (a) Gravimetric capacitance at different current densities calculated for the cell, (b) Ragone plot for WH–TiO_2/PPy.

storage and ion accessibility in the electrode material, further confirming the favorable electrochemical characteristics of the WH–TiO_2/PPy//AC composite.

Fig. 10(b) shows the Ragone plot, illustrating the relationship between specific energy and specific power at different constant current densities. The highest specific energy observed is 98 W h kg^{-1} at a power density of 3207 W kg^{-1}. Reviewing the results at the higher current density the specific energy is decreased and can be stated at 39 W h kg^{-1} as the maximum specific power of 5606 W kg^{-1}. This trend appears to be the usual trade-off in most of the supercapacitors where high power densities come associated with low energy densities. Taken together, these results clearly show that the proposed WH–TiO_2/PPy//AC asymmetric supercapacitor has high gravimetric capacitance, energy and power density as well as efficient ion transport capabilities. As a result, the developed WH–TiO_2/PPy composite exhibits both pseudocapacitive and EDLC performance with stable cycling and excellent rate capability delivering an excellent application performance for the energy storage devices.

4 Conclusion

The WH–TiO_2/PPy composite was successfully synthesized *via* hydrothermal treatment and interfacial polymerization, demonstrating a specific capacitance of 610 F g^{-1} at 0.5 A g^{-1}. The enhanced electrochemical performance is attributed to the synergistic effects of TiO_2 for improved ion transport, PPy for pseudocapacitive contribution with enhances conductivity, and the porous WH matrix for efficient charge storage. The asymmetric supercapacitor achieved an energy density of 98 W h kg^{-1} and a power density of 5606 W kg^{-1}, with over 80% capacitance retention after 5000 cycles, indicating long-term stability. Beyond supercapacitor applications, the utilization of *Eichhornia crassipes* presents a sustainable approach to biomass valorization. Future research should explore optimizing conductivity and structural stability, integrating bio-based dopants, and expanding its potential for environmental applications such as phytoremediation and wastewater treatment, further advancing green chemistry principles.

Data availability

The data that support the findings of this study are available from the corresponding author upon reasonable request.

Conflicts of interest

The authors declare that they have no known competing financial interests or personal relationships that could have appeared to influence the work reported in this paper.

Acknowledgements

Centre for Research, CHRIST University, for the financial support provided for this research work under project grant no: SMSS-2216.

References

1 Y. Z. Cai, Y. S. Fang, W. Q. Cao, P. He and M. S. Cao, MXene-CNT/PANI ternary material with excellent supercapacitive performance driven by synergy, *J. Alloys Compd.*, 2021, **868**, 159159, DOI: 10.1016/j.jallcom.2021.159159.
2 P. A. Owusu and S. Asumadu-Sarkodie, A review of renewable energy sources, sustainability issues and climate change mitigation, *Cogent Eng.*, 2016, **3**(1), DOI: 10.1080/23311916.2016.1167990.
3 T. Schoetz, L. W. Gordon, S. Ivanov, A. Bund, D. Mandler and R. J. Messinger, Disentangling faradaic, pseudocapacitive, and capacitive charge storage: A tutorial for the characterization of batteries, supercapacitors, and hybrid systems, *Electrochim. Acta*, 2022, **412**, 1–29, DOI: 10.1016/j.electacta.2022.140072.
4 S. Zhu, J. Ni and Y. Li, Carbon nanotube-based electrodes for flexible supercapacitors, *Nano Res.*, 2020, **13**(7), 1825–1841, DOI: 10.1007/s12274-020-2729-5.
5 L. Bach-Toledo, B. M. Hryniewicz, L. F. Marchesi, L. H. Dall'Antonia, M. Vidotti and F. Wolfart, Conducting polymers and composites nanowires for energy devices: A

Open Access Article. Published on 23 May 2025. Downloaded on 2/7/2026 11:23:07 PM. This article is licensed under a Creative Commons Attribution-NonCommercial 3.0 Unported Licence.

brief review, *Mater. Sci. Energy Technol.*, 2020, **3**, 78–90, DOI: 10.1016/J.MSET.2019.09.006.

6 N. James, S. Simon, S. Rajeevan, S. C. George and S. P. Balakrishnan, Symmetric Supercapacitors based on Reduced Graphene Oxide/Multi-walled Carbon Nanotubes/Cobalt Oxide Ternary Composites, *J. Macromol. Sci., Part B: Phys.*, 2023, 1–22, DOI: 10.1080/00222348.2023.2285656.

7 L. Luo, L. Shi, D. Lu and J. Z. B, Flexible and free-standing MXene decorated biomass-derived carbon cloth membrane anodes for superior lithium-ion capacitors, *J. Energy Storage*, 2024, **103**(part B), 114430, DOI: 10.1016/j.est.2024.114430.

8 Y. Li, M. S. Yao and Y. He, Recent Advances of Electrocatalysts and Electrodes for Direct Formic Acid Fuel Cells: from Nano to Meter Scale Challenges, *Nano-Micro Lett*, 2025, **17**, 148, DOI: 10.1007/s40820-025-01648-w.

9 X. Zheng, Z. Song, D. Zhang, *et al.*, Rational design of a dual-gradient zincophilic-conductive interphase for dendrite-free zinc batteries, *J. Mater. Chem. A*, 2024, **12**(25), 15352–15360, DOI: 10.1039/d4ta02639j.

10 P. Thomas, C. W. Lai and M. R. Bin Johan, Recent developments in biomass-derived carbon as a potential sustainable material for super-capacitor-based energy storage and environmental applications, *J. Anal. Appl. Pyrolysis*, 2019, **140**, 54–85, DOI: 10.1016/j.jaap.2019.03.021.

11 J. Wang, Q. Zhang and M. Deng, Eco-Friendly Preparation of Biomass-Derived Porous Carbon and Its Electrochemical Properties, *ACS Omega*, 2022, **7**(26), 22689–22697, DOI: 10.1021/acsomega.2c02140.

12 C. Huang, T. Sun and D. Hulicova-Jurcakova, Wide electrochemical window of supercapacitors from coffee bean-derived phosphorus-rich carbons, *ChemSusChem*, 2013, **6**(12), 2330–2339, DOI: 10.1002/cssc.201300457.

13 X. Du and Z. Wang, Effects of polymerization potential on the properties of electrosynthesized PEDOT films, *Electrochim. Acta*, 2003, **48**(12), 1713–1717, DOI: 10.1016/S0013-4686(03)00143-9.

14 S. Simon, P. Harikumar and P. B. Sreeja, Green Power: The Role of Plant-Based Biochar in Advanced Energy Storage, *ChemPhysChem*, 2024, 202400569, DOI: 10.1002/cphc.202400569.

15 S. Simon and P. B. Sreeja, Polyaniline/Reduced Graphene Oxide/Zinc Oxide Hybrid Electrodes Fabricate by Combining Electrospinning/Electrospray Technique for Supercapacitors, *J. Energy Storage*, 2024, **6**(8), 1–9, DOI: 10.1002/est2.70101.

16 A. Geim and K. Novoselov, The rise of graphene, *Nat. Mater.*, 2007, **6**, 183–191, DOI: 10.1038/nmat1849.

17 M. Jasna, M. Muraleedharan Pillai, A. Abhilash, P. S. Midhun, S. Jayalekshmi and M. K. Jayaraj, Polyaniline wrapped carbon nanotube/exfoliated MoS2 nanosheet composite as a promising electrode for high power supercapacitors, *Carbon Trends*, 2022, **7**, 100154, DOI: 10.1016/J.CARTRE.2022.100154.

18 J. P. Cheng, B. Q. Wang, S. H. Gong, X. C. Wang, Q. S. Sun and F. Liu, Conformal coatings of NiCo2O4 nanoparticles and nanosheets on carbon nanotubes for supercapacitor electrodes, *Ceram. Int.*, 2021, **47**(23), 32727–32735, DOI: 10.1016/j.ceramint.2021.08.169.

19 R. K. Gupta, *NanoCarbon: A Wonder Material for Energy Applications*, 2024, vol. 2, DOI: 10.1007/978-981-99-9931-6.

20 K. Naoi, W. Naoi, S. Aoyagi, J. I. Miyamoto and T. Kamino, New generation "nanohybrid supercapacitor.", *Acc. Chem. Res.*, 2013, **46**(5), 1075–1083, DOI: 10.1021/ar200308h.

21 X. Fan, C. Yu, J. Yang, *et al.*, A layered-nanospace-confinement strategy for the synthesis of two-dimensional porous carbon nanosheets for high-rate performance supercapacitors, *Adv. Energy Mater.*, 2015, **5**(7), 1–7, DOI: 10.1002/aenm.201401761.

22 Q. Lu, S. Zhou, Y. Zhang, M. Chen, B. Li, H. Wei, D. Zhang, J. Zhang, Q. Liu, *et al.*, Nanoporous carbon derived from green material by an ordered activation method and its high capacitance for energy storage, *Nanomaterials*, 2020, **10**(6), 1058, DOI: 10.3390/nano10061058.

23 Ş. Kılkış, G. Krajačić, N. Duić, M. A. Rosen and M. A. Al-Nimr, Advancements in sustainable development of energy, water and environment systems, *Energy Convers. Manag.*, 2018, **176**, 164–183, DOI: 10.1016/j.enconman.2018.09.015.

24 Y. Wang, Y. Zhang, L. Pei, *et al.*, Converting Ni-loaded biochars into supercapacitors: Implication on the reuse of exhausted carbonaceous sorbents, *Sci. Rep.*, 2017, **7**, 1–8, DOI: 10.1038/srep41523.

25 Q. V. Thi, Y. Lee, H. Y. Cho, *et al.*, Core-shell architecture of Ni-Co MOF wrapped by a heterogeneous FeBTC@PPy layer for high-performance EMI shielding, *Synth. Met.*, 2021, **281**, 116929, DOI: 10.1016/j.synthmet.2021.116929.

26 R. Turczyn, K. Krukiewicz, A. Katunin, J. Sroka and P. Sul, Fabrication and application of electrically conducting composites for electromagnetic interference shielding of remotely piloted aircraft systems, *Compos. Struct.*, 2020, **232**, 111498, DOI: 10.1016/j.compstruct.2019.111498.

27 B. Liu, H. Sun, T. Peng and X. Zhi, 3D core-shell poly(aniline-co-pyrrole)/reduced graphene oxide composite for supercapacitor performance, *Diam. Relat. Mater.*, 2021, **118**, 108498, DOI: 10.1016/j.diamond.2021.108498.

28 A. Baby, A. Saranraj, S. Abinaya, S. P. Jose, V. P. Aswathi and S. Puthenveetil Balakrishnan, Capacitive Behaviour of Imidazole Azo Modified Carbon Nanotubes/Polypyrrole Composite in Aqueous Electrolytes, *J. Electrochem. Soc.*, 2023, **170**(6), 060537, DOI: 10.1149/1945-7111/acdda1.

29 L. Sun, Z. Yin, J. Zhang, Z. Ren, M. Zhang, W. Song, Z. Xu, C. Qi, *et al.*, Gold nanoparticles supported on poly (aniline-co-pyrrole) as the efficient catalysts for the reduction of 4-nitrophenol, *Mol. Catal.*, 2022, **525**, 112362, DOI: 10.1016/j.mcat.2022.112362.

30 C. Peng, J. Jin and G. Z. Chen, A comparative study on electrochemical co-deposition and capacitance of composite films of conducting polymers and carbon nanotubes, *Electrochim. Acta*, 2007, **53**(2), 525–537, DOI: 10.1016/j.electacta.2007.07.004.

31 Z. Zhang, F. Xiao, Y. Guo, S. Wang and Y. Liu, One-Pot Self-Assembled Three-Dimensional TiO_2-Graphene Hydrogel, *ACS Appl. Mater. Interfaces*, 2013, **5**(6), 2227–2233.

© 2025 The Author(s). Published by the Royal Society of Chemistry

Open Access Article. Published on 23 May 2025. Downloaded on 2/7/2026 11:23:07 PM. This article is licensed under a Creative Commons Attribution-NonCommercial 3.0 Unported Licence.

32 D. Li and Y. Xia, Direct fabrication of composite and ceramic hollow nanofibers by electrospinning, *Nano Lett.*, 2004, **4**(5), 933–938, DOI: **10.1021/nl049590f**.

33 D. Li and Y. Xia, Fabrication of Titania Nanofibers by Electrospinning, *Nano Lett.*, 2003, **3**(4), 44, DOI: **10.1021/nl034039o**.

34 R. Chandrasekar, L. Zhang, J. Y. Howe, N. E. Hedin, Y. Zhang and H. Fong, Fabrication and characterization of electrospun titania nanofibers, *J. Mater. Sci.*, 2009, **44**(5), 1198–1205, DOI: **10.1007/s10853-008-3201-1**.

35 C. C. Raj and R. Prasanth, Review—Advent of TiO 2 Nanotubes as Supercapacitor Electrode, *J. Electrochem. Soc.*, 2018, **165**(9), E345–E358, DOI: **10.1149/2.0561809jes**.

36 A. Saning, S. Herou, D. Dechtrirat, *et al.*, Green and sustainable zero-waste conversion of water hyacinth (: Eichhornia crassipes) into superior magnetic carbon composite adsorbents and supercapacitor electrodes, *RSC Adv.*, 2019, **9**(42), 24248–24258, DOI: **10.1039/c9ra03873f**.

37 Y. Li and X. Liu, Activated carbon/ZnO composites prepared using hydrochars as intermediate and their electrochemical performance in supercapacitor, *Mater. Chem. Phys.*, 2014, **148**(1–2), 380–386, DOI: **10.1016/j.matchemphys.2014.07.058**.

38 M. Mirzaee, C. Dehghanian and K. Sabet Bokati, One-step electrodeposition of reduced graphene oxide on three-dimensional porous nano nickel-copper foam electrode and its use in supercapacitor, *J. Electroanal. Chem.*, 2018, **813**(2017), 152–162, DOI: **10.1016/j.jelechem.2018.02.032**.

39 R. Mondal, N. K. Mishra, T. Maiyalagan, A. Gupta and P. Singh, La1-xK xFeO3-δ: An Anion Intercalative Pseudocapacitive Electrode for Supercapacitor Application, *ACS Omega*, 2021, **6**(45), 30488–30498, DOI: **10.1021/acsomega.1c03902**.

40 R. Hajare, S. Kempahanumakkagaari, T. Ramakrishnappa, A. Saniya, K. Sourav and A. Amrutha, Study of advances in carbon composites as electrodes for supercapacitors, *Mater. Today Proc.*, 2022, **49**, 650–659, DOI: **10.1016/J.MATPR.2021.05.164**.

41 S. Sharma and P. Chand, Supercapacitor and electrochemical techniques: A brief review, *Results Chem.*, 2023, **5**, 100885, DOI: **10.1016/j.rechem.2023.100885**.

42 U. V. Shembade, S. R. Gurav, M. A. Gaikwad, *et al.*, Hydrothermal synthesis of graphene oxide interspersed in non-uniform tungsten oxide nanorod and its performance towards highly efficient hybrid supercapacitor, *Ceram. Int.*, 2024, **50**(1), 340–350, DOI: **10.1016/j.ceramint.2023.10.107**.

43 A. Yussuf, M. Al-Saleh, S. Al-Enezi and G. Abraham, Synthesis and Characterization of Conductive Polypyrrole: The Influence of the Oxidants and Monomer on the Electrical, Thermal, and Morphological Properties, *Int. J. Polym. Sci.*, 2018, **2018**, 9484, DOI: **10.1155/2018/4191747**.

44 D. J. G. Alzate, F. C. R. Peñafiel and C. A. Binag, Polypyrrole on pineapple (Ananas comosus) and water hyacinth (Eichhornia crassipes) polyester blended textiles as promising electrode materials for supercapacitor applications, *Mater. Chem. Phys.*, 2022, **279**, DOI: **10.1016/j.matchemphys.2022.125774**.

45 O. Nurhilal, S. Hidayat, D. Sumiarsa and R. Risdiana, Natural Biomass-Derived Porous Carbon from Water Hyacinth Used as Composite Cathode for Lithium Sulfur Batteries, *Sustain*, 2023, **15**(2), 1039, DOI: **10.3390/su15021039**.

46 W. N. Deng, Y. H. Li, D. F. Xu, W. Zhou, K. X. Xiang and H. Chen, Three-dimensional hierarchically porous nitrogen-doped carbon from water hyacinth as selenium host for high-performance lithium–selenium batteries, *Rare Met.*, 2022, **41**, 3432–3445, DOI: **10.1007/s12598-022-02022-0**.

47 F. Z. Yakdoumi and A. S. Hadj-Hamou, Effectiveness assessment of TiO2-Al2O3nano-mixture as a filler material for improvement of packaging performance of PLA nanocomposite films, *J. Polym. Eng.*, 2020, **40**(10), 848–858, DOI: **10.1515/polyeng-2020-0105**.

48 W. Yao, P. Liu, C. Liu, J. Xu, K. Lin, H. Kang, M. Li, X. Lan and F. Jiang, Flexible conjugated polyfurans for bifunctional electrochromic energy storage application, *Chem. Eng. J.*, 2022, **428**, 131125, DOI: **10.1016/j.cej.2021.131125**.

49 R. M. A. P. Lima, G. S. dos Reis, U. Lassi, E. C. Lima, G. L. Dotto and H. P. de Oliveira, Sustainable Supercapacitors Based on Polypyrrole-Doped Activated Biochar from Wood Waste Electrodes, *C*, 2023, **9**(2), 59, DOI: **10.3390/c9020059**.

50 M. Ates, S. Caliskan and M. Gazi, A ternary nanocomposites of graphene/TiO 2/polypyrrole for energy storage applications, *Fullerenes, Nanotub. Carbon Nanostruct.*, 2018, **26**(10), 631–642, DOI: **10.1080/1536383X.2018.1457651**.

51 T. Chen, Y. Liu, L. Pan, *et al.*, Electrospun carbon nanofibers as anode materials for sodium ion batteries with excellent cycle performance, *J. Mater. Chem. A*, 2014, **2**(12), 4117–4121, DOI: **10.1039/c3ta14806h**.

52 W. Li, C. Ni, H. Lin, C. P. Huang and S. I. Shah, Size dependence of thermal stability of TiO 2 nanoparticles, *J. Appl. Phys.*, 2004, **96**(11), 6663–6668, DOI: **10.1063/1.1807520**.

53 S. M. Matome, E. Makhado, L. M. Katata-Seru, *et al.*, Green synthesis of polypyrrole/nanoscale zero valent iron nanocomposite and use as an adsorbent for hexavalent chromium from aqueous solution, *S. Afr. J. Chem. Eng.*, 2020, **34**, 1–10, DOI: **10.1016/j.sajce.2020.05.004**.

54 M. Sahadat Hossain and S. Ahmed, Easy and green synthesis of TiO2 (Anatase and Rutile): Estimation of crystallite size using Scherrer equation, Williamson-Hall plot, Monshi-Scherrer Model, size-strain plot, Halder- Wagner Model, *Results Mater.*, 2023, **20**, 100492, DOI: **10.1016/j.rinma.2023.100492**.

55 Y. Masuda and K. Kato, Synthesis and phase transformation of TiO2 nano-crystals in aqueous solutions, *J. Ceram. Soc. Jpn.*, 2009, **117**(1363), 373–376, DOI: **10.2109/jcersj2.117.373**.

56 N. Jameel Z, J. Haider A and Y. Taha S, Synthesis of TiO2 Nan particles by Using Sol-Gel Method and Its Applications as Antibacterial Agents, *J. Eng. Technol.*, 2014, **32**(3B), 418–426, DOI: **10.30684/etj.32.3b.4**.

57 M. Šetka, R. Calavia, L. Vojkůvka, E. Llobet, J. Drbohlavová and S. Vallejos, Raman and XPS studies of ammonia

Open Access Article. Published on 23 May 2025. Downloaded on 2/7/2026 11:23:07 PM.
This article is licensed under a Creative Commons Attribution-NonCommercial 3.0 Unported Licence.

sensitive polypyrrole nanorods and nanoparticles, *Sci. Rep.*, 2019, **9**(1), 1–10, DOI: **10.1038/s41598-019-44900-1**.

58 J. Tabačiarová, M. Mičušík, P. Fedorko and M. Omastová, Study of polypyrrole aging by XPS, FTIR and conductivity measurements, *Polym. Degrad. Stab.*, 2015, **120**, 392–401, DOI: **10.1016/j.polymdegradstab.2015.07.021**.

59 G. Greczynski and L. Hultman, X-ray photoelectron spectroscopy: Towards reliable binding energy referencing, *Prog. Mater. Sci.*, 2020, **107**, 100591, DOI: **10.1016/j.pmatsci.2019.100591**.

60 D. Prashad Ojha, M. Babu Poudel and H. Joo Kim, Investigation of electrochemical performance of a high surface area mesoporous Mn doped TiO2 nanoparticle for a supercapacitor, *Mater. Lett.*, 2020, **264**, 127363, DOI: **10.1016/j.matlet.2020.127363**.

61 J. Paduraksa, M. Luthfi, A. Verdianto, *et al.*, Preparation of activated carbon derived from water hyacinth as electrode active material for li-ion supercapacitor, *Mater. Sci. Forum*, 2020, **1000**, 50–57, DOI: **10.4028/www.scientific.net/MSF.1000.50**.

62 K. Wu, B. Gao, J. Su, *et al.*, Large and porous carbon sheets derived from water hyacinth for high-performance supercapacitors, *RSC Adv.*, 2016, **6**(36), 29996–30003, DOI: **10.1039/c5ra25098f**.

63 K. Zheng, Y. Li, M. Zhu, *et al.*, The porous carbon derived from water hyacinth with well-designed hierarchical structure for supercapacitors, *J. Power Sources*, 2017, **366**, 270–277, DOI: **10.1016/j.jpowsour.2017.09.034**.

64 K. M. Shell, S. Y. Vohra, D. D. Rodene and R. B. Gupta, Phytoremediation of Nickel via Water Hyacinth for Biocarbon-Derived Supercapacitor Applications, *Energy Technol.*, 2021, **9**(8), 1–9, DOI: **10.1002/ente.202100130**.

65 W. Li, Y. Bu, H. Jin, *et al.*, The preparation of hierarchical flowerlike NiO/reduced graphene oxide composites for high performance supercapacitor applications, *Energy Fuels*, 2013, **27**(10), 6304–6310, DOI: **10.1021/ef401190b**.

66 S. Simon, N. James and P. B. Sreeja, Water hyacinth-poly(3,4-Ethylenedioxythiophene) composite as a facile electrode for supercapacitor application, *Mater. Today Proc.*, 2023, DOI: **10.1016/j.matpr.2023.10.068**.

67 H. Wei, Y. Wang, J. Guo, *et al.*, Electropolymerized Polypyrrole Nanocoatings on Carbon Paper for Electrochemical Energy Storage, *Chemelectrochem*, 2015, **2**(1), 119–126, DOI: **10.1002/celc.201402258**.

68 A. C. Lazanas and M. I. Prodromidis, Electrochemical Impedance Spectroscopy–A Tutorial, *ACS Meas. Sci. Au*, 2023, **3**(3), 162–193, DOI: **10.1021/acsmeasuresciau.2c00070**.

69 D. D. MacDonald, Reflections on the history of electrochemical impedance spectroscopy, *Electrochim. Acta*, 2006, **51**(8–9), 1376–1388, DOI: **10.1016/j.electacta.2005.02.107**.

70 R. Kumar, E. Joanni, S. Sahoo, *et al.*, An overview of recent progress in nanostructured carbon-based supercapacitor electrodes: From zero to bi-dimensional materials, *Carbon*, 2022, **193**, 298–338, DOI: **10.1016/j.carbon.2022.03.023**.

© 2025 The Author(s). Published by the Royal Society of Chemistry